9-1981

# Application of Adaptive Learning Networks to Quantitative Flaw Definition

M. F. Whalen
*Adaptronics, Inc.*

P. M. Garafola
*Adaptronics, Inc.*

L. J. O'Brien
*Adaptronics, Inc.*

Anthony N. Mucciardi
*Adaptronics, Inc.*

# Application of Adaptive Learning Networks to Quantitative Flaw Definition

**Abstract**
Adaptive Learning Networks (ALNs) are algebraic, nonlinear multinomials whose structure and coefficients are learned from empirical data. Over the past several years, their application to quantitative NDE problems has become widespread. The major advantage of the ALN approach is that only a modest data base of experiments is needed, from which the ALN models can be trained. In this work, ALNs are used as a nonlinear, empirical inversion procedure for various defect geometries. Measurements from a sparselypopulated ultrasonic transducer array are input to the ALNs which estimate the defect characteristics. The defects considered are (1) elliptical cracks, (2) irregular-shaped voids, and (3) surface-breaking semielliptical cracks. The models are synthesized from theoretically-generated, forward-scattering data, then evaluated on actual experimental data recorded from titanium and carbon steel samples. The advantage of using theoretical data to train the models is that ultrasonic responses can be generated quickly and inexpensively in a digital computer, thereby avoiding, or greatly minimizing, the expense of calibration sample fabrication. The size and orientation estimates for the experimental evaluation are in excellent agreement with the true defect characteristics.

**Keywords**
Nondestructive Evaluation

**Disciplines**
Materials Science and Engineering

# APPLICATION OF ADAPTIVE LEARNING NETWORKS TO QUANTITATIVE FLAW DEFINITION

M. F. Whalen
P. M. Garafola
L. J. O'Brien
A. N. Mucciardi

ADAPTRONICS, INC.
McLean, Virginia 22102

ABSTRACT

Adaptive Learning Networks (ALNs) are algebraic, nonlinear multinomials whose structure and coefficients are learned from empirical data. Over the past several years, their application to quantitative NDE problems has become widespread. The major advantage of the ALN approach is that only a modest data base of experiments is needed, from which the ALN models can be trained. In this work, ALNs are used as a nonlinear, empirical inversion procedure for various defect geometries. Measurements from a sparsely-populated ultrasonic transducer array are input to the ALNs which estimate the defect characteristics. The defects considered are (1) elliptical cracks, (2) irregular-shaped voids, and (3) surface-breaking semielliptical cracks. The models are synthesized from theoretically-generated, forward-scattering data, then evaluated on actual experimental data recorded from titanium and carbon steel samples. The advantage of using theoretical data to train the models is that ultrasonic responses can be generated quickly and inexpensively in a digital computer, thereby avoiding, or greatly minimizing, the expense of calibration sample fabrication. The size and orientation estimates for the experimental evaluation are in excellent agreement with the true defect characteristics.

## 1. SUMMARY OF RESULTS, CONCLUSIONS, AND RECOMMENDATIONS

### RESULTS

During this year's effort, Adaptive Learning Networks (ALNs) were synthesized to estimate the size and orientation of elliptical cracks and to estimate the depth of free-surface cracks. Other objectives were to evaluate the oblate spheroid models developed last year on extrapolative data, and to catalog all important models synthesized to date under the DARPA/AFML program. Table 1.1 summarizes the performance of each of these models on theoretically generated training data.

TABLE 1.1: ALN MODEL PERFORMANCE SUMMARY

| Defect Type | Estimated Parameter | Relative Error |
|---|---|---|
| Elliptical Crack | Semiminor Axis (A) | 22% |
| Elliptical Crack | Semimajor Axis (B) | 13% |
| Elliptical Crack | Polar Angle ($\alpha$) | 5% |
| Elliptical Crack | Azimuthal Angle ($\beta$) | 10% |
| Elliptical Crack | Rotation ($\gamma$) | 21% |
| Free-Surface Crack | Depth | 6% |
| Oblate Spheroid | Minor Radii (A) | 9% |
| Oblate Spheroid | Major Radii (B) | 8% |
| Oblate Spheroid | Polar Angle ($\alpha$) | 5% |
| Oblate Spheroid | Azimuthal Angle ($\beta$) | 1% |
| Crack vs. Void | Defect Type | 0% |

The error of each of these models, when evaluated on experimentally recorded data, were very similar to the errors based on theoretical data.

It was found that the "ripple frequency" feature of the power spectrum contained considerable information about the size of elliptical and free-surface cracks. The low frequency energy content was found to be indicative of size for the void defects. The spatial distribution of total power was key in estimating the orientation for both crack and void defects. The standard deviation of the power spectrum was an important feature in discriminating cracks from voids.

The oblate spheroid models were evaluated on four defect types, none of which were included in the training data set. These defect types, along with the qualitative estimates of how the models performed in estimating their size and orientation, are summarized in Table 1.2.

TABLE 1.2: SUMMARY OF OBLATE SPHEROID ALN MODEL PERFORMANCE ON EXTRAPOLATION DATA

| Defect Type | Estimate Size | Estimate Orientation |
|---|---|---|
| Prolate Spheroid | Excellent | Excellent |
| Grooved Oblate | Good | Good |
| Sphere with Ring | Fair | Good |
| Lumpy Sphere | Fair | Poor |

The "good" and "excellent" estimates on the prolate and grooved oblate spheroids demonstrate the extrapolative qualities of the ALN solution. The less favorable estimates on the sphere with ring and lumpy sphere indicate the need to develop a generalized solution for complex shapes. Section 5 presents both a graphical and a numerical presentation of the estimated defect sizes and orientations.

### CONCLUSIONS AND RECOMMENDATIONS

The inversion of various crack and void defect types, as listed in Table 1.1, can be achieved with a high degree of accuracy via ALN modeling techniques. Additionally, these models perform well when evaluated on defect types unseen during the modeling synthesis. The parameters estimated

for voids (A, B, $\alpha$, and $\beta$) may not have been fully adequate to estimate the more complex defect shapes like the lumpy sphere. It is, therefore, recommended that a more sophisticated parameter set for complex shapes be determined in future efforts.

Both two-dimensional and three-dimensional versions of Achenbach's free-surface forward-scattering theory for semielliptical cracks were investigated in this effort. A favorable match was obtained between theory and experiment for the two-dimensional case only. Consequently, the 2-D theory was used for data base generation. The 3-D theory should be compared against more experimental data as they become available.

The Weiner method for deconvolving the transducer reference from the experimental ultrasonic data is an optimum procedure. This method was employed to deconvolve all of the experimental analyzed data and the process was extremely stable.

The hexagonal array used in this work provided uniform coverage of the spheroid trailer-hitch samples over a wide aperture with a minimum number of elements. This array structure can also be extended to more common part geometries.

Calculation of the "ripple frequency" was accomplished by computing the power spectrum on a power spectrum after subtraction of the spectral envelope. The envelope subtraction was essential to remove the low-quefrency trend in the first spectrum. This method yielded consistently good results for both the theoretical and experimental data.

The forward-scattering theory for the elliptical crack was further verified by comparison to experimental data.

Before further inversions of complex cracks and voids are pursued, a mathematical means for representing these shapes must be defined. Estimation of simple parameters such as A, B, $\alpha$, and $\beta$ for complex voids seems to have yielded only marginal results. One recommendation for future work is to estimate the coefficients on a spherical harmonic expansion. There are, however, other ways for representing complex shapes in space, and the method which offers the highest correlation between the scattered ultrasonic field and the defect parameter should be used. Once this mathematical structure is defined, a more ubiquitous ALN inversion model should be derived which performs on both simple and complex shapes and possibly cracks as well as voids.

## 2. INTRODUCTION

Adaptronics became a contributor to the Interdisciplinary Program for Quantitative Flaw Definition in 1976 after the Second Year Effort. During the first three years, ALNs were successfully applied to the investigation of simple geometries such as spheroidal-shaped voids and elliptical crack defects, both in free space [1, 2, 3]. The ALN models were trained directly from theoretically generated data and evaluated in blind tests on experimentally recorded defect samples.

In the present effort, more realistic defect geometries have been considered. A free-surface crack model has been obtained which measures the depth of surface-connected cracks. Also, last year's oblate spheroid ALN models were evaluated this year with several complex-shaped defects to determine their extrapolative qualities. These defect shapes included: (1) the sphere with ring; (2) lumpy sphere; (3) grooved oblate spheroid; and (4) the prolate spheroid. Additionally, the elliptical-crack ALN models from last year were retrained to include "$\gamma$" the third orientation parameter. In last year's effort, this angle was assumed to be zero. A section summarizing all inputs and ALN models synthesized under the DARPA/AFML project is included in this report.

As in the previous three-year effort, the ALN models were trained on theoretically generated forward-scattering data and the inversion algorithms evaluated on both theoretical and experimentally recorded data.

The advantage of training the ALN models with theoretical data is that the scattered field from many defect geometries can be produced quickly and at a fraction of the cost of what is required to fabricate physical defect calibration specimens. The theoretical data have the added advantage of being noise-free. Ultimately, as the theories become more sophisticated, mimicking complicated defect shapes, surface roughness, multiple defects, and flaws in the vicinity of geometrical reflectors, data bases for field and industrial use can be generated entirely in a digital computer. This data base can always be augmented with experimental data from real flaws as it becomes available. The ultimate goal of Adaptronics, with regard to the Interdisciplinary Program, is to develop a generalized ALN model which can be used to invert either simple or complex shapes without the need to retrain the model each time a new defect category is considered. Recent advances in the development of accurate forward-scattering theories allow this goal to be entirely achievable in the very near future.

A block diagram illustrating the overall Adaptronics project philosophy is shown in Figure 2.1. The forward-scattering theories which generated the theoretical training data bases were provided by J. Achenbach, et al., and V. Varadan, for crack-defects and void-defects, respectively. An ALN synthesis program inputted the theoretical data bases to produce the ALN models. These models were evaluated on both theoretical and experimental data. All experimental data were recorded by J. Martin of the Rockwell Science Center. Other contributors were E. Domany, H. McMaken, A. Norris, and B. Tittman.

## 3. DEVELOPMENT OF ELLIPTICAL CRACK MODELS

### DEFECT GEOMETRY

An elliptical-shaped crack oriented at an arbitrary position in space can be represented by two radii (A and B), and three orientation parameters ($\alpha$, $\beta$, and $\gamma$).

For the purposes of this study, we assumed these parameters to be defined as follows:

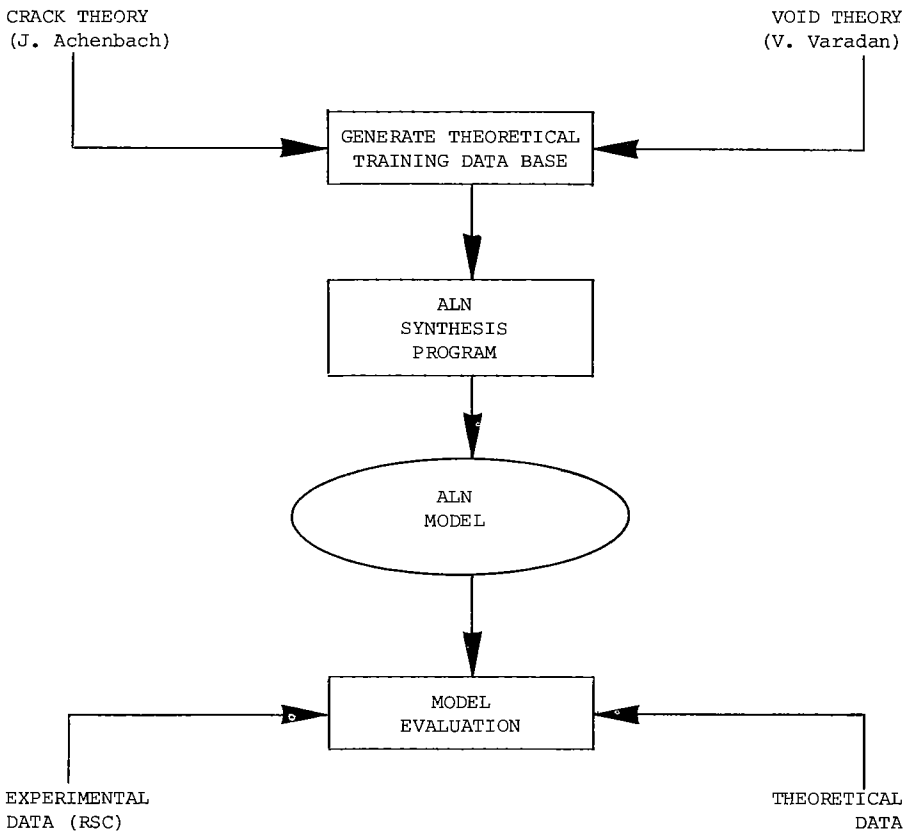


FIGURE 2.1: PROJECT PHILOSOPHY

A - Radius of the minor axis
B - Radius of the major axis
$\alpha$ - First Euler-angle rotation
$\beta$ - Second Euler-angle rotation
$\gamma$ - Third Euler-angle rotation

The Euler-angle rotations are defined in Figure 3.1. The first rotation is around the Z-axis; the second rotation is around the new major axis (line of nodes); and the third rotation is around the defect normal.

The Euler rotations are taken to be in the positive counterclockwise direction, and when all three angles are zero, the major axis, B, is assumed to lie along the positive X direction, and the minor axis, A, is assumed to lie along the positive Y direction. This defines a right-handed coordinate system in which the normal to the defect (M in Figure 3.1) lies along the Z-axis. This vertical axis also defines the center position of the receiver.

## ARRAY CONFIGURATION

A 19-element hexagonal array was used to measure the scattered field. This array is illustrated in Figure 3.2. The transducer angular positions are defined in Table 3.1. Data were recorded in the pitch-catch mode with the center element acting as the transmitter. All 19 elements served as receivers. Only the L→L mode responses were considered. The mode-converted shear wave response was gated out of the recorded echo transients. The 19 receivers formed a 120° cone-shaped aperture with the transmitter at the cone center.

For the theoretical data, the scattering amplitudes were generated at the 19 positions given in Table 3.1 for each defect specified. This provided 19 different "views" of the elliptical crack over a wide aperture. The defect was assumed to be positioned at the origin. A hexagonally-spaced array is advantageous since all elements are equally spaced. On the surface of a sphere, each element is exactly 30° from its adjacent elements.

## THEORETICAL DATA BASE

A computer code representing a far-field approximation to the geometrical theory of diffraction has been developed by Northwestern University for use by Adaptronics in calculating estimates of the power spectrum recorded at a particular location where an input ultrasonic signal is diffracted from a defect of specified geometry. The derivation of this model has been discussed extensively and has been shown to be in favorable agreement with experimental results [4, 5].

TABLE 3.1: RECEIVER ORIENTATION ANGLES

| Receiver Number | Polar Angle "θ" (Degrees) | Azimuthal Angle "φ" (Degrees) |
|---|---|---|
| 1 | 30 | 30 |
| 2 | 30 | 90 |
| 3 | 30 | 150 |
| 4 | 30 | 210 |
| 5 | 30 | 270 |
| 6 | 30 | 330 |
| 7 | 52 | 0 |
| 8 | 52 | 60 |
| 9 | 52 | 120 |
| 10 | 52 | 180 |
| 11 | 52 | 240 |
| 12 | 52 | 300 |
| 13 | 60 | 30 |
| 14 | 60 | 90 |
| 15 | 60 | 150 |
| 16 | 60 | 210 |
| 17 | 60 | 270 |
| 18 | 60 | 330 |
| * 19 | 0 | 0 |

* Both Transmit and Receive

Theoretical power spectra corresponding to longitudinal mode scattering were generated at each receiver point in the 19-element array using the pitch-catch operating mode with the transmitter located at the center of the array. A total of 22,680 possible experiments were considered and are identified in Table 3.2. To reduce repetition in the data, a random number generator was used to randomly select 7 percent of the 22,680 possible experiments. This resulted in the generation of 1,625 actual cases, broadly distributed across the values listed in Table 3.2. Synthetic spectra were obtained for 14 different defect sizes (A and B), 9 different values of $\alpha$, 15 different values of $\beta$, and 12 different values of $\gamma$. The frequency band of interest was from 1.0 to 9.0 MHz with a frequency resolution of 0.20 MHz. The corresponding ka range of the data was from 0.31 to 22.3.

## EXPERIMENTAL DATA BASE

The experimental data for training the theoretically trained ALN models were collected at the Rockwell Science Center from a set of known specimens. Defects were machined at the center of titanium hemispheres, which were then diffusion-bonded together to form a sphere. The receiver array shown in Figure 3.2 was placed on the sphere surface. The sample was rotated to simulate various defect orientations. For a comparison of theory and experiment, and for verification of the ability of ALNs to accurately predict sizes and orientations, four experiments were analyzed. The four included three separate orientations of an elliptical yttria disk of dimensions 1.285 millimeters x 0.705 millimeters with a thickness or depth of less than 0.050 millimeters, and one orientation of a cylindrical yttria disk of 1.425 millimeters x 1.425 millimeters, with a depth of less than 0.050 millimeters. The four experiments are summarized in Table 3.3. Figures 3.3 and 3.4 depict the geometry of the two defects.

## DECONVOLUTION

Deconvolution of ultrasonic signals is necessary to remove the specific transducer characteristics and to expand the data bandwidth. This is accomplished by dividing the complex spectrum of the data by a complex reference spectrum. The problem with a division is that it often leads to instability in the quotient function near the band limits. A Weiner deconvolution process was used in this work:

$$D(f) = \frac{X(f)R^*(f)}{|R(f)|^2 + |N(f)|^2} \qquad (3.1)$$

where

$D(f)$ = complex deconvolved spectrum
$X(f)$ = complex data spectrum
$R(f)$ = complex reference spectrum
$R^*(f)$ = complex conjugate of R
$N(f)$ = noise spectrum

In most applications, the noise spectrum is fairly uniform at all frequencies, hence, $|N(f)|$ can be replaced with a constant factor "$\epsilon$".

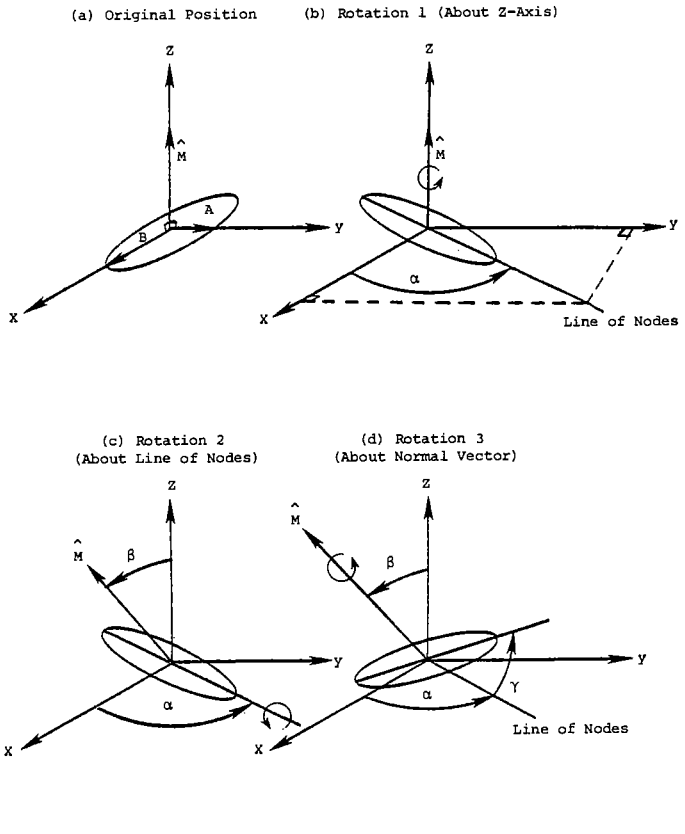


FIGURE 3.1: DEFINITION OF THREE EULER ANGLES TO DESCRIBE ORIENTATION OF ELLIPTICAL CRACK

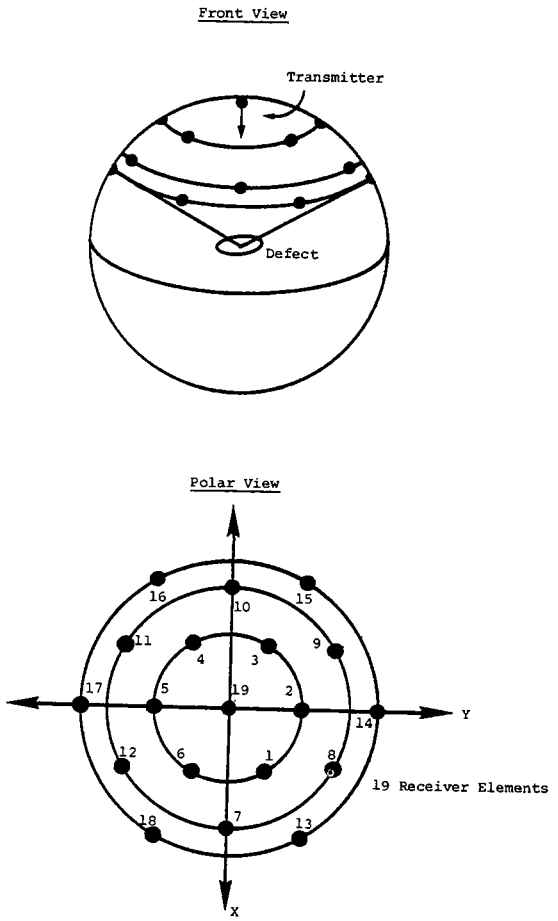


FIGURE 3.2: THE 19-ELEMENT HEXAGONAL ARRAY STRUCTURE

TABLE 3.2: RANGE OF VARIABLE VALUES IN THEORETICAL DATA BASE

| Defect Sizes | | | | | |
|---|---|---|---|---|---|
| | Crack Radii | | | Crack Radii | |
| No. | A(mm) | B(mm) | No. | A(mm) | B(mm) |
| 1 | .312 | .312 | 8 | .625 | 2.500 |
| 2 | .312 | .625 | 9 | 1.250 | 1.250 |
| 3 | .312 | 1.250 | 10 | 1.250 | 1.875 |
| 4 | .312 | 2.500 | 11 | 1.250 | 2.500 |
| 5 | .625 | .625 | 12 | 1.875 | 1.875 |
| 6 | .625 | 1.250 | 13 | 1.875 | 2.500 |
| 7 | .625 | 1.875 | 14 | 2.500 | 2.500 |

Orientation Angles (°)

Alpha (9 cases)

= 1, 10, 20, 30, 40, 50, 60, 70, 80

Beta (15 cases)

= 0, 25, 50, 75, 100, 125, 150, 175, 200, 225, 250, 275, 300, 325, 350

Gamma (12 cases)

= 0, 15, 30, 45, 60, 75, 90, 105, 120, 135, 150, 165

Possible Number of Experiments

14 sizes x 9 Alphas x 15 Betas x 12 Gammas = 22,680

TABLE 3.3: EXPERIMENTAL DEFECTS AND ORIENTATIONS

| Experiment Number | Defect Sizes (mm) | | | Orientations (Degrees) | | |
|---|---|---|---|---|---|---|
| | A | B | C | α | β | γ |
| 1 | 1.425 | 1.425 | <50 | 0 | 0 | 0 |
| 2 | 1.285 | .705 | <50 | 0 | 0 | 0 |
| 3 | 1.285 | .705 | <50 | 15 | 0 | 0 |
| 4 | 1.285 | .705 | <50 | 15 | 0 | 90 |

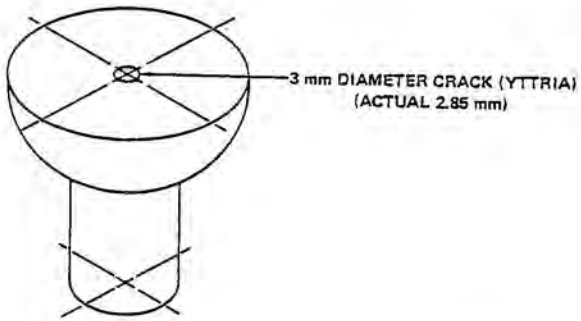


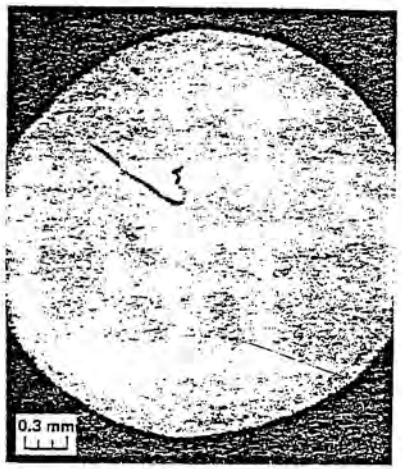


FIGURE 3.3: CRACK GEOMETRY FOR EXPERIMENT 1

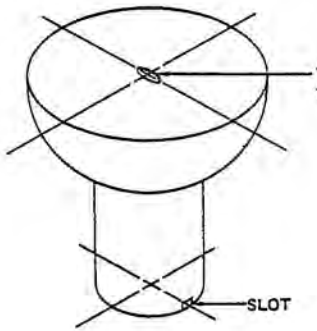



FIGURE 3.4: CRACK GEOMETRY FOR EXPERIMENTS 2, 3, AND 4

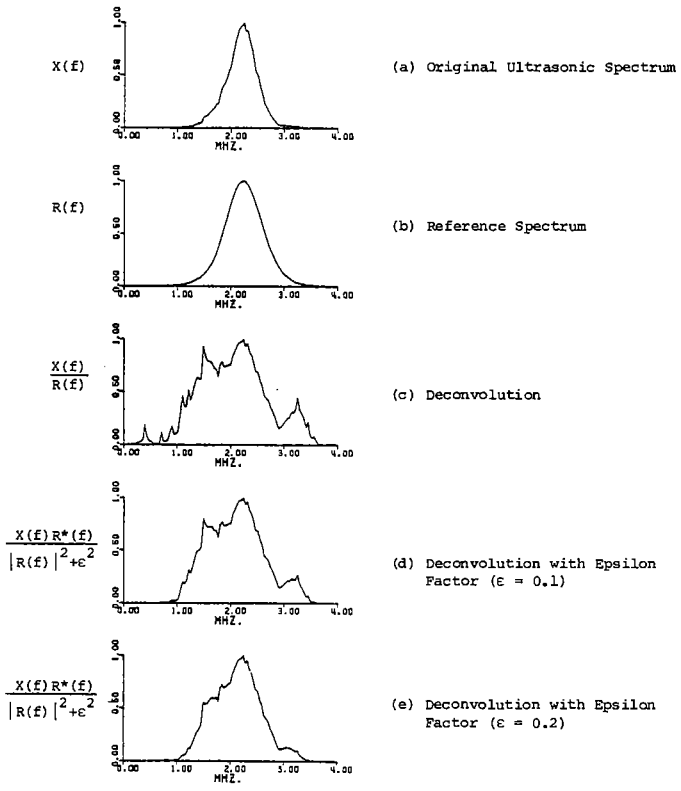


FIGURE 3.5: DEMONSTRATION OF THE WEINER DECONVOLUTION PROCESS

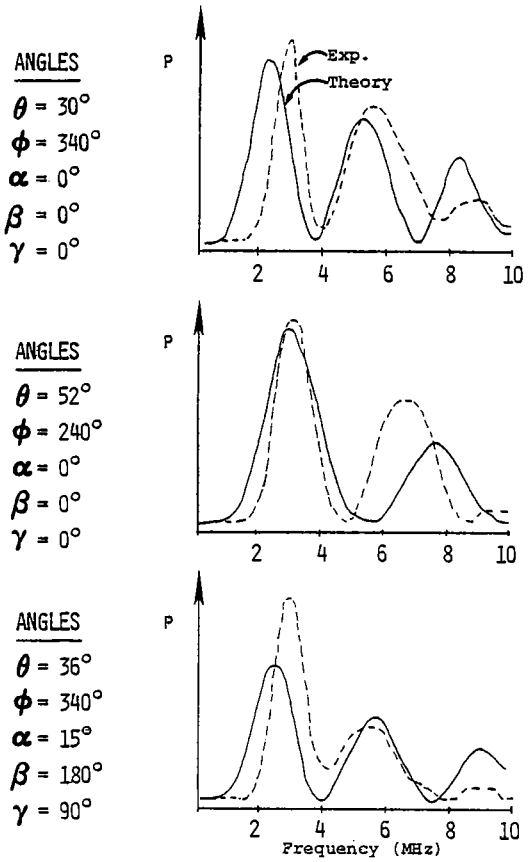


FIGURE 3.6: COMPARISON OF THE THEORETICAL AND EXPERIMENTAL ELLIPTICAL-CRACK POWER SPECTRA (A = .705 mm; B = 1.285 mm)

This method has recently been tested on ultrasonic crack data. The results were quite satisfactory. Figure 3.5 shows the power spectrum of a pulse-echo waveform (a); a reference spectrum (b); and three deconvolved spectra (c, d, and e) where Equation (3.1) was applied for three values of ($\varepsilon$ = 0.0, 0.1, and 0.2 times the peak reference power spectrum). When $\varepsilon$ = 0, the Weiner method becomes a simple division. Note how stable the deconvolved spectra are for $\varepsilon$ = 0.1 and $\varepsilon$ = 0.2. Also note the tendency toward instabilities when $\varepsilon$ = 0. All experimental data were deconvolved using the Weiner filter.

## COMPARISON OF THEORY AND EXPERIMENT

The theoretical elliptical-crack forward-scattering model, provided by Achenbach and McMaken, yielded a far-field physical elastodynamic approximate solution valid in the high ka regime (ka >> 1). Successful comparisons of theory and experiment have been provided in several other works [4, 5]. The most dominant characteristics of the scattered power spectrum is the successive pattern of peaks and troughs occurring at a single rate which shall be called the "ripple frequency." The rippling is caused by interface patterns due to the delayed arrivals of the diffracted waves from the near and far edge of the crack. The ripple frequency was found to be the single most important feature for determining crack size.

In comparing the theoretical spectra to the experimental data collected by Rockwell, several cases were in close agreement with regard to the ripple frequency. This is seen in Figure 3.6 where the parameters of each experiment are listed. The major notable difference between the two spectra types is that the experimental data are attenuated in the higher frequencies. However, no action was taken in the present work to correct this deficiency since the causes of the attenuation are not completely known.

For as many cases which compared favorably, there were at least as many cases which compared poorly. This fact is associated with the difficulty in fabricating controlled defect samples and in collecting noise-free ultrasonic data.

## FEATURE EXTRACTION

The ALN synthesis process requires that candidate features be computed from each of the training experiments. In developing the model, the training algorithm determines which features are significant, the weighting coefficients, and the nonlinear multinomial structure. Unimportant features are automatically discarded from consideration.

Two spectral features were computed from each of the 19 receiver power spectra. These were the total power between 1.0 and 9.0 MHz and the ripple frequency. From each spectral feature, a group of 20 spatial features were computed over the 19 receiver locations. A total of 40 candidate features were therefore available for ALN synthesis.

The ripple frequency was determined by taking a power spectrum of the power spectrum and noting the position of the maximum peak. The envelope was subtracted from the first power spectrum to suppress the dominant low-quefrency artifact. This method yielded consistently good ripple frequency estimates for both the theoretical and experimental data; Figure 3.7 illustrates this process. The ripple frequency ($\tau$) has the units of time. This can be converted to a distance measure by multiplying by the longitudinal wave propagation velocity.

The 20 spatial features computed from both the total spectral power and the ripple frequency are defined in Table 3.4. The first nine features are the coefficients of the generalized three-dimensional second-order surface:

$$w_1x^2 + w_2y^2 + w_3z^2 + w_4xy + w_5xz + w_6yz + w_7x + w_8y + w_9z = 1 \qquad (3.2)$$

which best fit through each of the 19 receiver locations. The method of least squares was used to determine the w's. Features #10, 11, and 12 are, respectively, the x, y, and z components of the moment vector of the 19 observations, which is characteristic of the polar orientation of the crack. The four arctangent features (13-16) further characterize the orientation of the defect, and the last four features are the four invariants of the second-order surface, given by the following equations:

$$I_1 = w_1 + w_2 + w_3 \qquad (3.3)$$

$$I_2 = w_1w_2 + w_1w_3 + w_2w_3 - w_4^2 - w_5^2 - w_6^2 \qquad (3.4)$$

$$I_3 = \begin{vmatrix} w_1 & w_4 & w_5 \\ w_4 & w_2 & w_6 \\ w_5 & w_6 & w_7 \end{vmatrix} \qquad (3.5)$$

$$I_4 = \begin{vmatrix} w_1 & w_4 & w_5 & w_7 \\ w_4 & w_2 & w_6 & w_8 \\ w_5 & w_6 & w_3 & w_4 \\ w_7 & w_8 & w_9 & -1 \end{vmatrix} \qquad (3.6)$$

Mathematically, the invariant features are insensitive to rotations of the measured field. Therefore, these features should have been good size estimators. However, the ALN training procedure did not select any of these as informative features.

## ALN MODEL RESULTS

Five ALN models were synthesized on the theoretical forward-scattering data to estimate the five defect size and orientation parameters (A, B, $\alpha$, $\beta$, $\gamma$). The model structures and coefficients are given in Section 6. Each of the models were evaluated on approximately 1000 theoretical experiments and the four experimentally recorded cases described above. The theoretical results are summarized in Table 3.5.

TABLE 3.5: ELLIPTICAL-CRACK INVERSION RESULTS

(Evaluation on theoretical data)

| Parameter | Relative Error |
|---|---|
| A | 21.8% |
| B | 12.6% |
| $\alpha$ | 5.0% |
| $\beta$ | 9.6% |
| $\gamma$ | 21.5% |

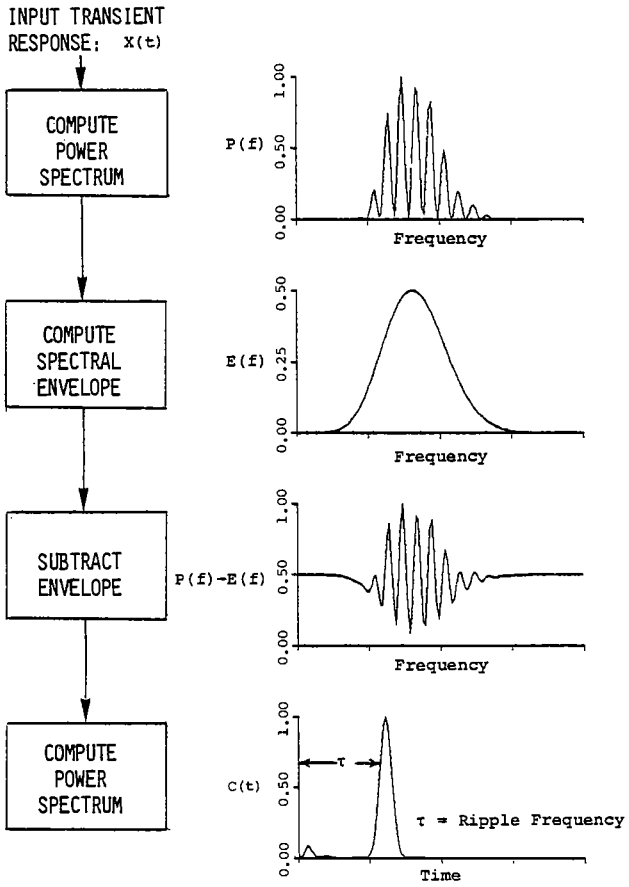


FIGURE 3.7: RIPPLE FREQUENCY CALCULATION

TABLE 3.4: DEFINITION OF THE CANDIDATE SPATIAL FEATURES

| Feature Number | Symbol | : | Description |
|---|---|---|---|
| 1 | $w_1$ | : | $x^2$ coefficient of the second-order surface |
| 2 | $w_2$ | : | $y^2$ coefficient of the second-order surface |
| 3 | $w_3$ | : | $z^2$ coefficient of the second-order surface |
| 4 | $w_4$ | : | xy coefficient of the second-order surface |
| 5 | $w_5$ | : | xz coefficient of the second-order surface |
| 6 | $w_6$ | : | yz coefficient of the second-order surface |
| 7 | $w_7$ | : | x coefficient of the second-order surface |
| 8 | $w_8$ | : | y coefficient of the second-order surface |
| 9 | $w_9$ | : | z coefficient of the second-order surface |
| 10 | $\bar{x}$ | : | $\frac{1}{N}\sum_{1}^{19} F_i \sin\theta_i \cos\phi_i$ * |
| 11 | $\bar{y}$ | : | $\frac{1}{N}\sum_{1}^{19} F_i \sin\theta_i \sin\phi_i$ |
| 12 | $\bar{z}$ | : | $\frac{1}{N}\sum_{1}^{19} F_i \cos\theta_i$ |
| | | | $(\bar{x}, \bar{y}, \bar{z})$ = Centroid or Moment Vector of $F_i$ |
| 13 | ATAN1 | : | $\tan^{-1}(\bar{y}/\bar{x})$ |
| 14 | ATAN2 | : | $\tan^{-1}((\bar{x}^2 + \bar{y}^2)/\bar{z}^2)$ |
| 15 | ATAN3 | : | $\tan^{-1}(w_2/w_1)$ |
| 16 | ATAN4 | : | $\tan^{-1}((w_1 + w_2)/w_3)$ |
| 17 | $I_1$ | : | first invariant of the second-order surface |
| 18 | $I_2$ | : | second invariant of the second-order surface |
| 19 | $I_3$ | : | third invariant of the second-order surface |
| 20 | $I_4$ | : | fourth invariant of the second-order surface |

* $F_i$ is the total power or ripple frequency computed at the $i^{th}$ receiver position; $\theta_i$ and $\phi_i$ are the polar and azimuthal angles of the $i^{th}$ receiver position.

The best results were obtained for the orientation parameters $\alpha$ and $\beta$. Poorer but still respectable results were obtained for the semi-minor axis, "A", and the orientation angle "$\gamma$". The angle, $\gamma$, measured the rotation of the defect about its normal. Defects having an aspect ratio close to one produced only subtle changes in the scattered ultrasonic field for varying cases of $\gamma$. These subtle changes were difficult to model with the sparsely populated 19-element array. Furthermore, "$\gamma$" is not defined for circular defects.

It was noted from the theoretical data analysis that the model error was a function of the defect size. For the ALNs which estimated A and B as the defects became smaller, the size became more difficult to estimate. An explanation of this can be linked to the ripple frequency calculation. Although the power spectrum method of computing the ripple frequency worked well when two or more ripples were present, this technique could not accurately resolve the ripple frequency when fewer than two ripples were present. (This is another way of stating that a wider bandwidth is needed.) Also, power spectra having a fractional number of ripples would be resolved to the nearest integer. For instance, a spectrum with 1.4 ripples would be resolved as having a ripple frequency of 1.0. It is, therefore, understandable that the ALN model to estimate the smaller-size parameter (A) would yield a larger error. It was noted that if the smaller defects ($A < 0.625$ mm) were eliminated from the evaluation set, the error for "A" dropped from 21.8 percent to 13.4 percent.

The ALN model results for the four experimental samples are given in Figure 3.8. The true defect size is illustrated to scale along with the estimated defect size. Note that the agreement is quite favorable. The orientation error shown in the last column gives the angle between the true defect normal and the estimated defect normal. Note again that the errors in three of the four cases are very small. The experimental results for estimation of the third angle, $\gamma$, were very poor and, consequently, are not shown. It is believed that the subtle changes introduced in the ultrasonic scattering amplitudes by the existence of $\gamma$ were less than the irreducible error in the ultrasonic measurements. The orientation error in Figure 3.7 was computed only from $\alpha$ and $\beta$.

## 4. DEVELOPMENT OF FREE-SURFACE CRACK MODELS

The majority of the defect characterization work performed in the past few years under this program has been concerned with the development of general inversion procedures which are applicable to flaws occurring in free space. A number of models have been proposed recently which offer the possibility of extending these inversion techniques to cracks attached to a free surface [6, 7]. The purpose of this section is to synthesize ALN models using these new theoretical formulations and to evaluate the resulting networks using experimental observations.

The approach taken in this analysis is shown in block-diagram form in Figure 4.1. The theoretical free-surface crack models can be divided into two separate cases - one representing the two-dimensional problem and the other corresponding to the three-dimensional situation. For the purposes of this study, these two geometrical cases were considered independently. A data base of theoretical approximations was generated for each appropriate model and subjected to various feature extraction operations. These candidate features were then input to ALN models to determine the key parameters as well as the functional relationship between the defect characteristic and these key features. The performance of these models was then assessed by using experimental data collected from a series of fabricated free-surface cracks.

### THEORETICAL DATA BASE

The free-surface crack models used in this study represent solutions for a homogeneous, isotropic, linear elastic half-plane which contains a normal edge crack [7, 8]. The geometrical properties of the two cases are illustrated in Figure 4.2. In the two-dimensional situation, the crack is defined to possess a depth, "d", in the half-plane. The crack has a length, "l", and depth, "d", in the three-dimensional model. The models assume that a time-harmonic elastic wave is incident upon the crack and then obtains the total field in the half-plane by means of the linear superposition of the incident fields and the scattered fields. The solutions considered in this study represent far-field approximations corresponding to longitudinal mode scattering.

### TWO-DIMENSIONAL FREE-SURFACE CRACK MODELING

A computer code representing the two-dimensional free-surface model was prepared by Northwestern University and used by Adaptronics to generate a number of power spectra corresponding to longitudinal mode pulse-echo recordings over the frequency range from 0.5 to 2.5 MHz. A suite of these spectra obtained for various crack depths is shown in Figure 4.3. For comparison purposes, each of these spectral plots was normalized to a maximum power of unity so that characteristic spectral shapes could be determined visually. It can be seen that the ripple frequency (defined in the previous section) changes quite dramatically from approximately 1.6 MHz at a depth of 2 mm to 1.1 MHz at a 5 mm depth. It is interesting to note that this observation is consistent with the results presented in the previous discussion concerning the ripple period structure of the semielliptical cracks. Other observations which can be made based on the spectra presented in Figure 4.3 concern the distributions of relative power levels in certain frequency bands depending on defect depth. In general, as the defect depth increases, there appears to be an increase in the relative power distributions at the higher frequency levels.

In order to verify that the trends observed in these theoretical spectra are meaningful features for defect inversion exercises, it is necessary to determine how well these theoretically generated quantities conform to experimental observations. To satisfy this requirement, ultrasonic pulse-echo recordings were collected from a series of semi-elliptical free-surface defects fabricated in a carbon steel calibration test block. The experimental setup is shown in Figure 4.4. The transducer used in this collection exercise was characterized by a 1.0 MHz center frequency with 100% bandwidth and was used in the pulse-echo mode.

| EXP. NO. | TRUE SIZE (MM) | EST. SIZE (MM) | ORIENT. ERROR (DEGS) |
|---|---|---|---|
| 1 |  .705 x 1.285 |  .869 x 1.519 | 1/ 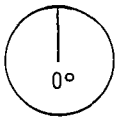 0° TRUE α = 0 β = - EST. α = 0 β = - |
| 2 |  .705 x 1.285 |  .645 x 1.117 | 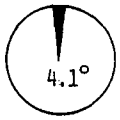 4.1° TRUE α = 15 β = 180 EST. α = 12 β = 169 |
| 3 |  .705 x 1.285 |  .518 x 1.147 | 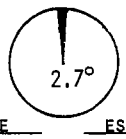 2.7° TRUE α = 15 β = 180 EST. α = 16 β = 170 |
| 4 | 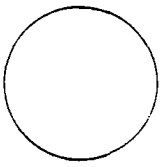 1.425 x 1. 425 |  .82 x 1.5 | 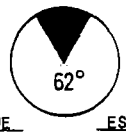 62° TRUE α = 0 β = - EST. α = 62 β = - |

1/ ORIENTATION ERROR = $\cos^{-1}\left[x_{true}x_{est} + y_{true}y_{est} + z_{true}z_{est}\right]$

FIGURE 3.8: ELLIPTICAL CRACK INVERSION RESULTS (EXP. DATA)

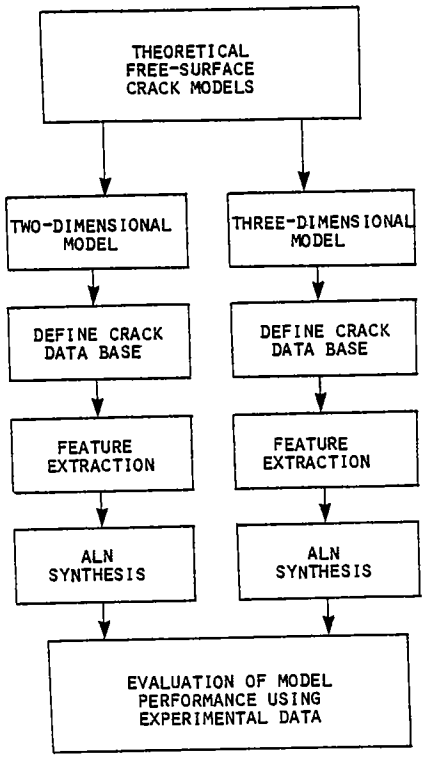


FIGURE 4.1: OVERVIEW OF THE ANALYSIS STEPS INVOLVED IN THE FREE-SURFACE CRACK MODEL STUDY

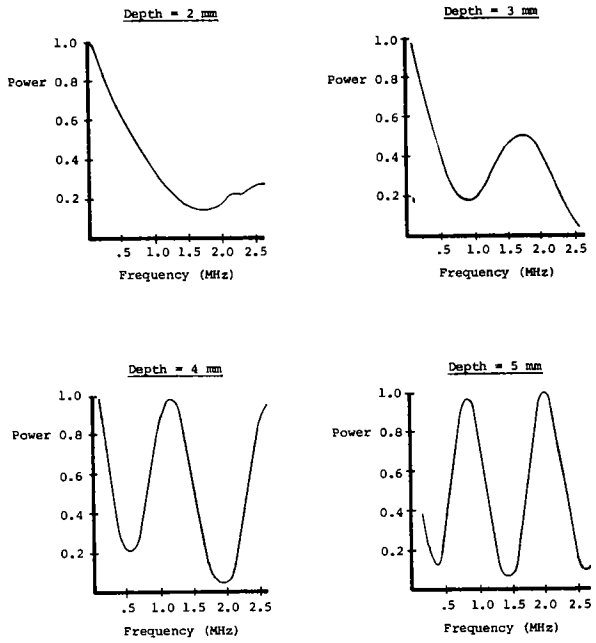


FIGURE 4.3: PULSE-ECHO POWER SPECTRAL L→L BULK WAVE RESPONSES FROM ACHENBACH'S TWO-DIMENSIONAL FREE-SURFACE SEMI-ELLIPTICAL CRACK THEORY (Incident Wave is 45°)

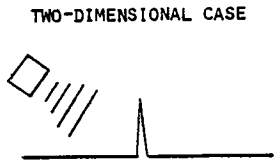


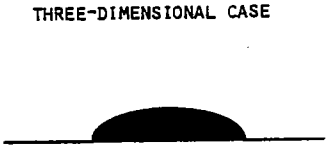


FIGURE 4.2: GEOMETRICAL REPRESENTATIONS OR THE TWO-DIMENSIONAL AND THREE-DIMENSIONAL FREE-SURFACE CRACKS

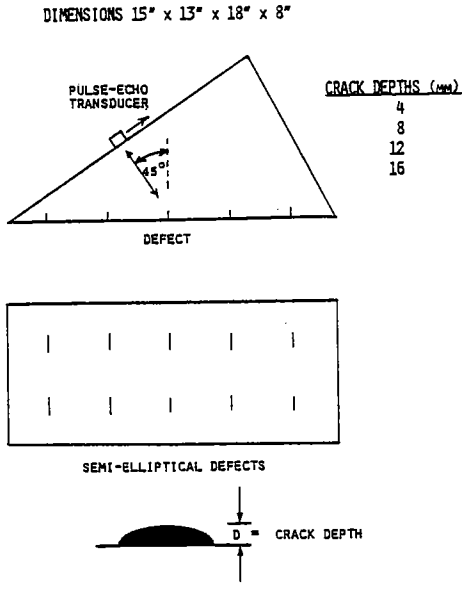


FIGURE 4.4: GEOMETRICAL DESCRIPTION OF THE EXPERIMENTAL DATA COLLECTION EXERCISE

The geometrical configuration of the test specimen enabled a 45° longitudinal wave to be emitted to the test block. A back-wall response was collected and used as a reference signal for deconvolution purposes.

The procedures employed in the data-collection exercises involved manual positioning of the transducer along the 45° edge of the test block to maximize the echo returned from the defect under analysis. Subsequent recordings were then obtained at a spacing of 6 mm in order to simulate a linear array. A total of six individual recordings were made moving up the edge of the calibration block. A comparison of theoretical and experimental power spectra is shown in Figure 4.5 for defect depths of 4, 8, and 12 mm. The transducer location for these spectra corresponds to a position 6 mm away from the direct corner reflection location. The experimental spectra have been deconvolved using the back-wall return as a reference. It can be seen that comparison is quite good for the 8 and 12 mm-deep cracks. Both the ripple periods and power distributions match up well over the frequency band from 0.5 to 2.0 MHz. The comparison presented for the 4 mm case is not as good as that for the larger defects and is probably related to the fact that the theoretical model does not perform well in the small ka region.

A more detailed comparison of the theoretical and experimental spectra obtained at the first four positions in the synthetic array is shown in Figures 4.6 - 4.8 for defect depths of 4, 8, and 12 mm. As noted previously, the comparisons are quite good for the larger defects and are less favorable for the smallest defect depth.

Based upon the close agreement obtained between the theoretical two-dimensional model and the experimental recordings, ALN models were synthesized to estimate the crack depth. The theoretical training data base consisted of ten crack depths and an array of six pulse-echo receivers. The specifics of the training set are described in Table 4.1. These theoretical spectra were then subjected to a number of feature extraction algorithms to determine candidate parameters to input to the ALN depth model. The candidate set consisted of eight individual quantities which are identified in Table 4.2. The features include the ripple period, measurements of power decay across the pulse-echo array, and various ratios of power levels in certain frequency bands.

TABLE 4.1: DATA BASE USED IN TRAINING ADAPTIVE LEARNING NETWORKS (Two-Dimensional Case)

DEFECT DEPTHS (MM)

4, 5, 6, 7, 8, 9, 10, 12, 14, 16

RECEIVERS

6 RECEIVERS OPERATING IN THE PULSE/ECHO MODE SEPARATED BY 6MM (LINEAR ARRAY)

TABLE 4.2: CANDIDATE FEATURES USED IN THE SYNTHESIS OF THE TWO-DIMENSIONAL FREE-SURFACE CRACK MODEL

1 - RIPPLE FREQUENCY

2 - DECAY OF TOTAL POWER FROM 0.5 - 2.5 MHZ

3 - DECAY OF TOTAL POWER FROM 0.5 - 1.5 MHZ

4 - DECAY OF TOTAL POWER FROM 1.5 - 2.5 MHZ

5 - DECAY OF AVERAGE POWER FROM 0.5 - 2.5 MHZ

6 - RATIO OF POWER IN BAND FROM 0.5 - 1.5 MHZ TO POWER IN BAND FROM 1.5 - 2.5 MHZ

7 - RATIO OF POWER IN BAND FROM 1.5 - 2.5 MHZ TO POWER IN BAND FROM 0.5 - 2.5 MHZ

8 - RATIO OF POWER IN BAND FROM 0.5 - 1.5 MHZ TO POWER IN BAND FROM 0.5 - 2.5 MHZ

The resulting ALN model is shown in Figure 4.9 and consists of two input features - the ripple frequency and the slope of the power decay across the six-element array over the frequency band from 0.5 to 1.5 MHz. The average relative error in the defect depth estimate was less than 6%. A scatter plot of the observed and predicted defect depth values is shown in Figure 4.10. The performance of the model was assessed using subsets of the experimental observations discussed previously in this section. The ripple period and power decay parameters were obtained from the observed spectral quantities and input to the ALN model to obtain estimates of crack depth. The results of this analysis are summarized in Table 4.3. The large error for the 4-mm defect has been discussed earlier and is probably a result of extending the theoretical model to small ka regions. The depth estimates for the 8-mm and 12-mm defects are very good with errors of less than 3% being observed.

TABLE 4.3: ALN MODEL PERFORMANCE

| TRUE CRACK DEPTH | ALN ESTIMATED CRACK DEPTH |
|---|---|
| 4.00 MM | 5.88 MM |
| 8.00 MM | 7.81 MM |
| 12.00 MM | 12.34 MM |

## THREE-DIMENSIONAL FREE-SURFACE CRACK MODELING

A computer code representing the three-dimensional free-surface crack model was prepared by Northwestern University and used by Adaptronics to generate a number of power spectra corresponding to longitudinal mode pulse-echo and pitch-catch recordings. An example of spectra obtained from a single pitch-catch arrangement for a series of different crack sizes is shown in Figure 4.11. The source position used in this illustration represents a polar angle of 45° and an azimuthal angle of 0° with reference to the crack. The reciever location is defined with a polar angle of 45° and azimuthal angle of 60°. It can be seen from this figure that, as the defect size increases, the spectral peaks shift to lower frequency levels. The ripple frequency characteristic of the spectrum appears to become greater as the defect size increases.

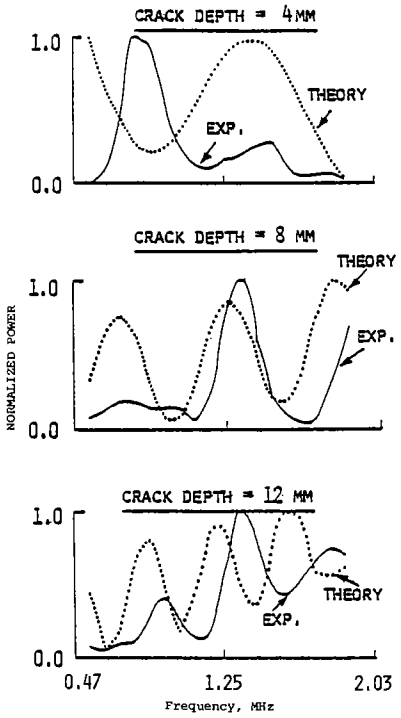


FIGURE 4.5: COMPARISON OF THEORETICAL AND EXPERIMENTAL POWER SPECTRA OBTAINED FOR VARIOUS CRACK DEPTHS

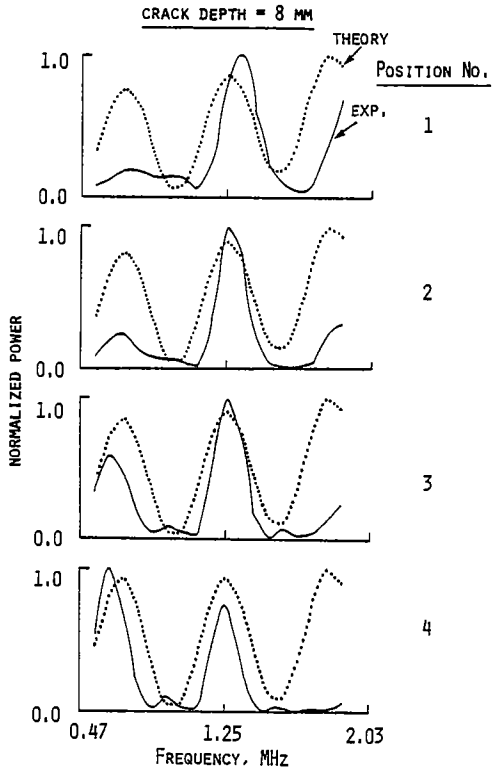


FIGURE 4.7: COMPARISON OF THEORETICAL AND EXPERIMENTAL POWER SPECTRA OBTAINED AT VARIOUS POSITIONS ON THE CALIBRATION BLOCK

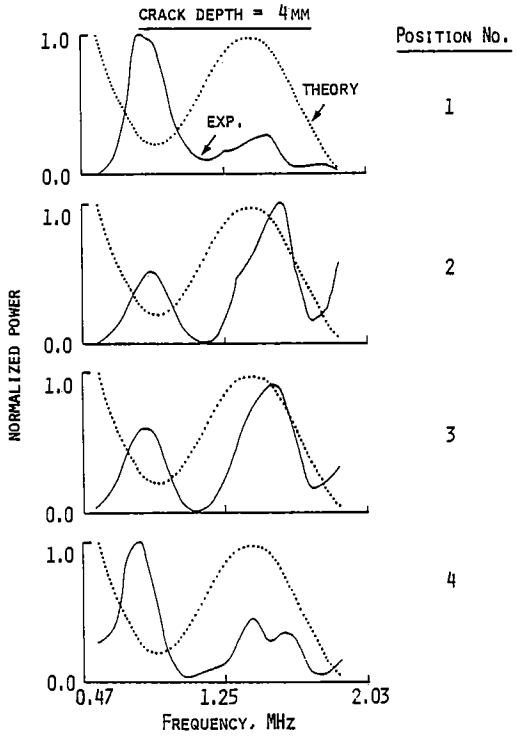


FIGURE 4.6: COMPARISON OF THEORETICAL AND EXPERIMENTAL POWER SPECTRA OBTAINED AT VARIOUS POSITIONS ON THE CALIBRATION BLOCK

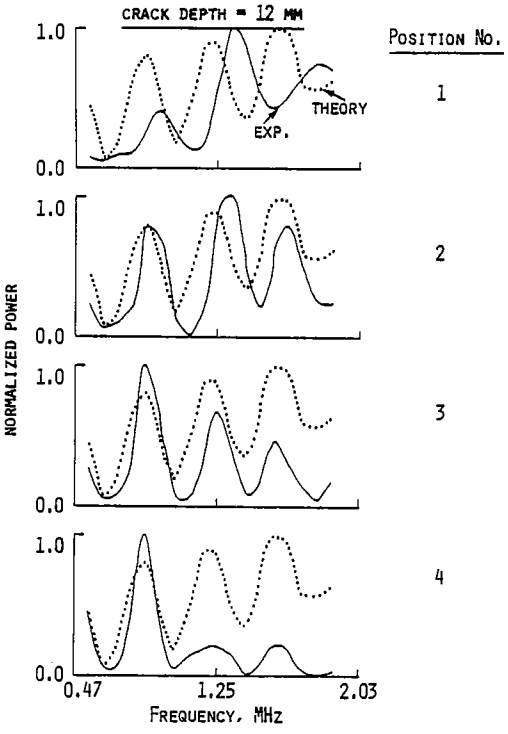


FIGURE 4.8: COMPARISON OF THEORETICAL AND EXPERIMENTAL POWER SPECTRA OBTAINED AT VARIOUS POSITIONS ON THE CALIBRATION BLOCK

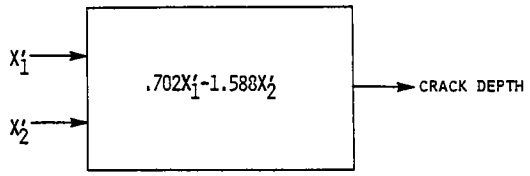


$X_1$ = SLOPE OF POWER DECAY ACROSS ARRAY IN BAND FROM 0.5 TO 1.5 MHz

$X_2$ = RIPPLE FREQUENCY

WHERE $X_N' = \frac{X_N - \mu_N}{\sigma_N}$, $\mu_N$ = MEAN, $\sigma_N$ = STANDARD DEVIATION

$\mu_1 = -.1545, \sigma_1 = .01463$

$\mu_2 = .5800, \sigma_2 = .23719$

FIGURE 4.9: ALN MODEL TO PREDICT CRACK DEPTH (Two-Dimensional Case)

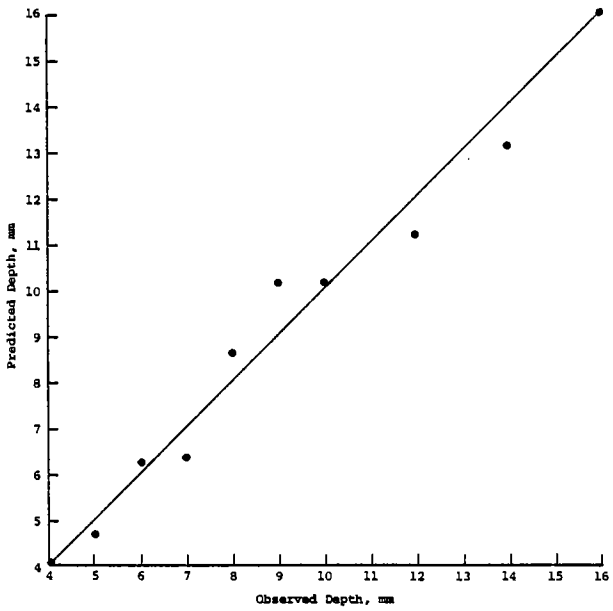


FIGURE 4.10: COMPARISON OF OBSERVED AND PREDICTED DEPTH VALUES FOR THE TWO-DIMENSIONAL MODEL

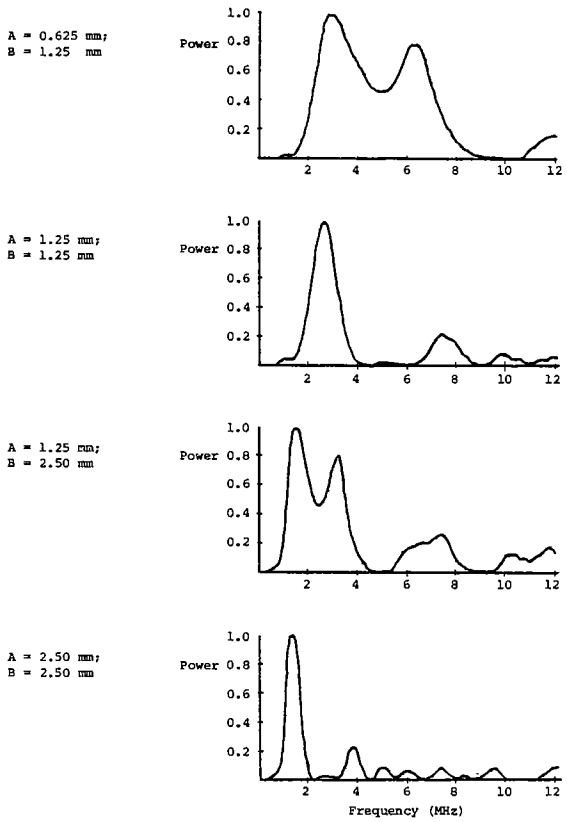


FIGURE 4.11: PITCH-CATCH POWER SPECTRAL L→L BULK WAVE RESPONSES FROM ACHENBACH'S THREE-DIMENSIONAL SEMIELLIPTICAL CRACK THEORY ($\theta_I = 45°$, $\phi_I = 0°$; $\theta_R = 45°$, $\phi_R = 60°$; A = half-length, B = depth.)

Following the procedures outlined in the two-dimensional model discussion, the next step involves a direct comparison of theoretical and experimental data. This requirement is satisfied in Figures 4.12 and 4.13 for a crack of depth 2.4 mm and of length 2.6 mm. The experimental data were collected by the Rockwell Science Center and forwarded to Adaptronics for analysis. The comparison illustrated in Figure 4.12 corresponds to a series of pulse-echo recordings obtained at various locations around the defect origin. In this case, the theoretical spectra were convolved with a back-wall reference recording to enable a quick comparison to be made. Over the frequency range from 5 to 12 MHz, it can be seen that the experimental spectra are characterized by a much higher oscillatory behavior than the theoretical spectra, leading to the conclusion that the ripple frequencies of the two spectra are not very comparable. This same general conclusion can be inferred from a comparison of the pitch-catch spectra shown in Figure 4.13. It is also noted that the actual power distributions are not in very good agreement over various frequency intervals. The reasons for the disagreements reported in this comparison have not been identified with any degree of certainty at this time and could probably be resolved by more comparison studies. Unfortunately, no other experimental observations are available to enable these discrepancies to be identified. Additional uncertainties associated with the true size of the defect used in this single experimental setup further cloud the comparison [9].

Based on these unresolved problems concerning the comparison of the theoretical and experimental three-dimensional crack spectra, the decision was made to defer the ALN analysis of this case until further investigations could be performed.

## 5. EVALUATION OF COMPOUND VOID MODELS WITH EXTRAPOLATION DATA

### SUMMARY

During last year's DARPA/AFML program, Adaptronics developed four ALN inversion models to estimate the size and orientation of oblate spheroid-shaped defects. The details of this work are covered in Reference [3]. In summary, a 19-element pulse-echo hexagonal array, whose receiver location matched those shown in Table 3.1, was used to capture the scattering amplitudes. A theoretical data base was generated from the T-Matrix theory to train the four ALN models. The models estimated the two radii of the spheroid (A and B), and two orientation angles ($\alpha$ and $\beta$). These geometrical descriptors are shown in Figure 5.1. The features to train the models were computed from the power spectrum and the characteristic function. Spatial features, similar to those discussed in the above sections, were computed from the spectral features. The model errors, when evaluated on independent theoretical data, were as follows:

| Parameter | Relative Error |
|---|---|
| A | 9% |
| B | 8% |
| $\alpha$ | 5% |
| $\beta$ | 1% |

The structures and coefficients of the four ALN models are given in Section 6.

### RESULTS

One objective of this year's effort was to evaluate the oblate spheroid ALN models, discussed above, with experimental data of more complex defect shapes. The point of this evaluation was to determine how the ALN models would perform on defects which were not represented in the training data set as a means of qualifying the extrapolative qualities of the models. Four classes of complex defects were evaluated:

(1) Prolate spheroid
(2) Grooved oblate spheroid
(3) Sphere with ring
(4) Lumpy sphere

Experimental pulse-echo waveforms were recorded on each of the four defect categories at several different orientations. These experimental RF transients were recorded at Rockwell Science Center on the trailer-hitch samples and were provided to Adaptronics for further processing. The hexagonal array element spacing was maintained. Fourier transforms and features were computed and the features were processed through the four ALN models. The results are shown both graphically and numerically in Figures 5.2 - 5.5.

The best results were obtained on the prolate spheroids (Figure 5.2). The true prolate size was A = 800 microns and B = 400 microns. This defect was viewed from two different orientations as shown. The true size is indicated by solid lines on the left side of Figure 5.2. The estimated defect size is represented by the broken lines. The two dimensions (A and B) are illustrated as the major and minor axis of an ellipse in the figure. Both the true and estimated sizes are shown numerically in microns. Note that, for both cases, the true and estimated sizes are very close. The true orientations of the two experiments were:

$\alpha = 15, \beta = 90$; and
$\alpha = 30, \beta = 90$.

The estimated orientations were:

$\hat{\alpha} = 21, \hat{\beta} = 94$; and
$\hat{\alpha} = 34, \hat{\beta} = 92$.

Figure 5.2 shows the orientation error which is the angle between the true defect normal and the estimated defect normal. This angle ($\psi$) was computed as:

$$\psi = \cos^{-1}(X_T X_E + Y_T Y_E + Z_T Z_E) \qquad (5.1)$$

where
$X = \sin\alpha \cos\beta$
$Y = \sin\alpha \sin\beta$
$Z = \cos\alpha$
T = "true"
E = "estimated"

The orientation error is shown as the "blacked-in" portion of the circle on the right side of Figure 5.2. Note that these errors are very small.

The evaluation results for the grooved oblate spheroid are shown in Figure 5.3. The format is the same as that described for Figure 5.2. In this case, three orientations of the same defect were considered. The true defect size was 195

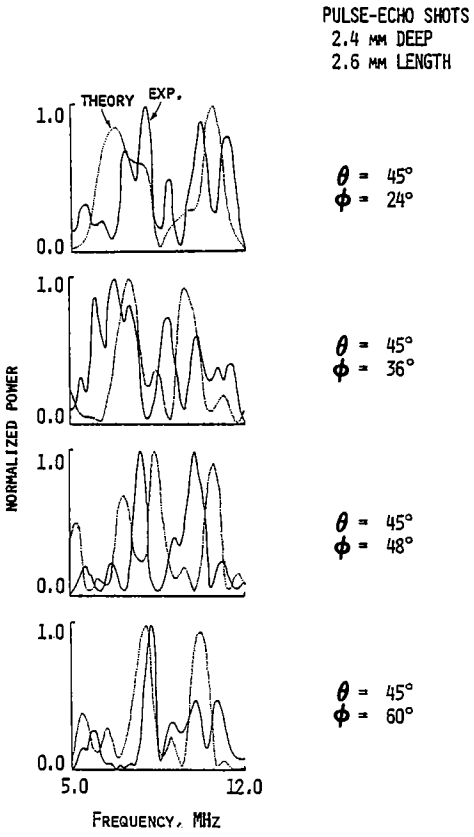


FIGURE 4.12: FREE-SURFACE ELLIPTICAL CRACK SPECTRA (Three-Dimensional Theory)

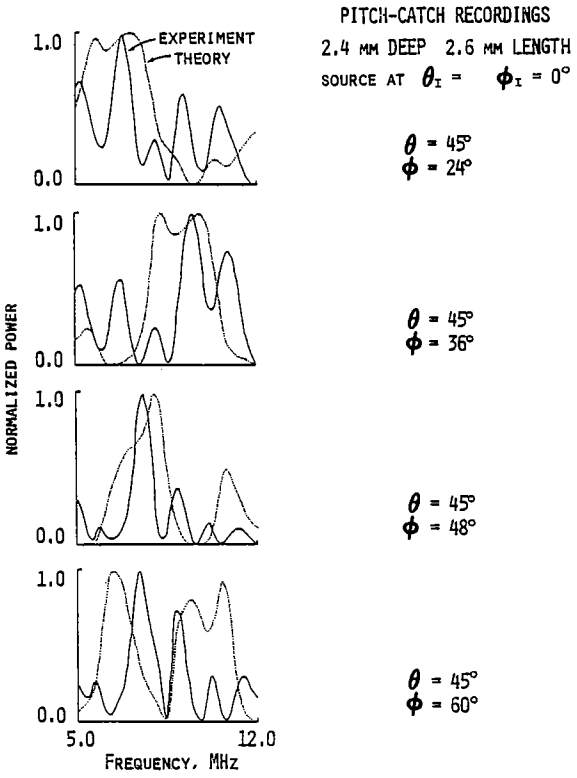


FIGURE 4.13: FREE-SURFACE CRACK SPECTRA (Three-Dimensional Theory)

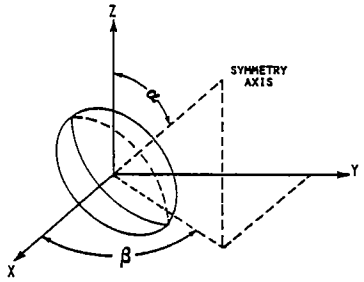


FIGURE 5.1: OBLATE SPHEROID COORDINATE GEOMETRY

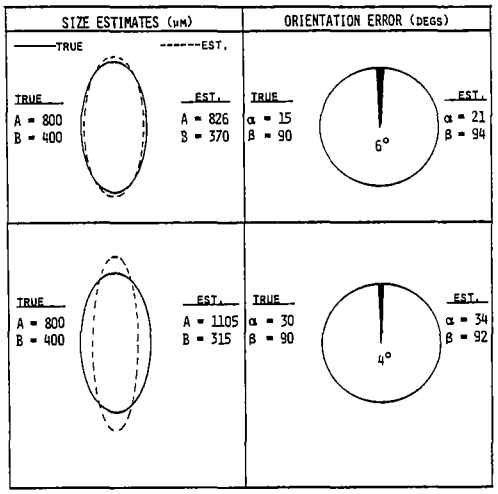


FIGURE 5.2: PROLATE SPHEROID ALN ESTIMATES

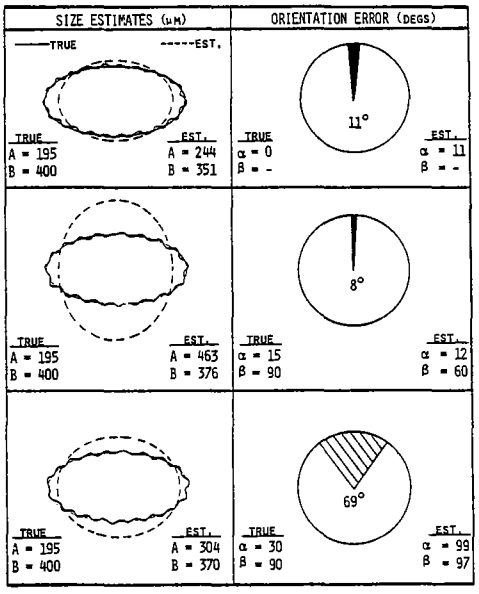


FIGURE 5.3: GROOVED OBLATE SPHEROID ALN ESTIMATES

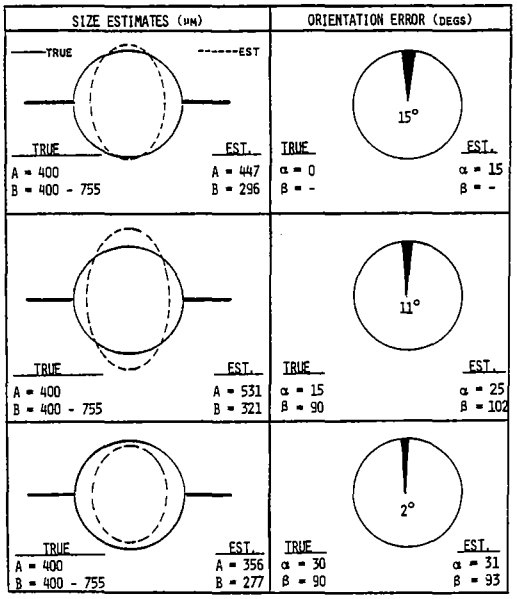


FIGURE 5.4: SPHERE WITH RING ALN ESTIMATES

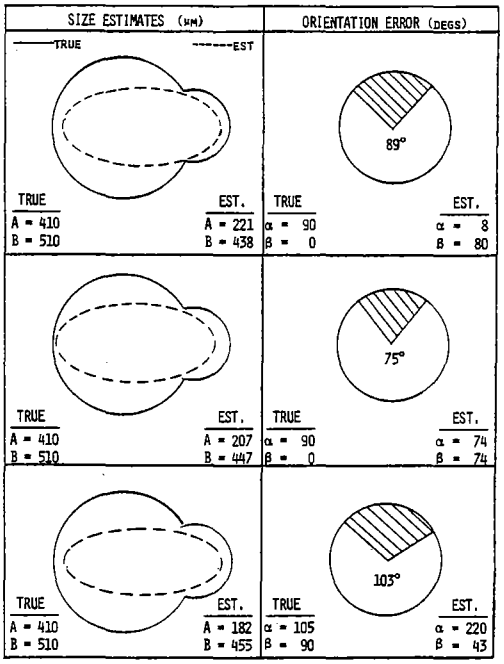


FIGURE 5.5: LUMPY SPHERE ALN ESTIMATES

microns by 400 microns. Small grooves of approximately one micron in depth were machined over the entire surface of the spheroid. The polar orientations ($\alpha$) of the defect were 0, 15, and 30 degrees. The azimuthal orientations ($\beta$) were at 90 degrees for two of the cases, as shown. Estimates for two of the three sizes were very close to the true values. The size estimate for the third defect was very good for the B dimension but about twice the true value for the A dimension, making the overall estimated shape of the defect appear slightly prolate. Two of the three orientation estimates were also quite good as indicated in Figure 5.3.

The next defect tested was the sphere with a ring. This defect was formed by diffusion-bonding the 400-micron hemispheres. An yttria disbonding agent was applied before diffusion to create a 755-micron ring similar to the "Ring of Saturn" but touching the sphere at its equator. The defect simulates a crack in the presence of a void. Data were recorded on three orientations. As indicated in Figure 5.4., each of the size estimates were very close to the actual size of the sphere, but the ring appeared to go undetected. The estimated shapes of all three cases were "egg-shaped." All of the orientation estimates were very close to the true values.

Figure 5.5 presents the true and estimated sizes and orientations for the lumpy sphere. This defect was formed by combining two spheres of unequal size ($R_1$ = 410 microns, $R_2$ = 200 Microns) such that the center of the smaller sphere was located at the surface of the larger sphere. The shape of the estimated defect in all three cases was that of an oblate spheroid. The overall estimated defect length was about equal to the true length. In general, the estimated defect size was slightly smaller than that of the lumpy sphere. The orientation errors for all three cases were large. This was probably due to the irregular reflecting surface of the defect, or due to the irreducible error associated with collecting experimental data.

Table 5.1 summarizes the results of this section in a qualitative fashion. The ability of the ALN models, trained only on theoretical oblate spheroid data, to characterize the experimentally-obtained, complex-shaped defects is rated in four categories: excellent, good, fair, and poor.

TABLE 5.1: SUMMARY OF OBLATE SPHEROID ALN MODEL PERFORMANCE ON EXTRAPOLATIVE DATA

| Defect Type | Estimate Size | Estimate Orientation |
|---|---|---|
| Prolate Spheroid | Excellent | Excellent |
| Grooved Oblate | Good | Good |
| Sphere with Ring | Fair | Good |
| Lumpy Sphere | Fair | Poor |

Overall, the ALN models performed quite well when one considers the differences between the training data and the evaluation data:

(1) The training data were theoretically generated, where the evaluated data were experimentally collected.

(2) The training defect types were different from the evaluation defect types.

(3) The training data were noise-free where the evaluation data contained noise.

Additionally, it should be mentioned that all model estimates were the same order of magnitude as the true defect sizes. No "blown-up" outputs resulted.

The results presented in this section demonstrate the extrapolative capabilities of ALN models applied to NDE methods. The fact that some of the defect estimates possessed larger-than-desirable errors can be more directly attributed to the inappropriate type of parameters modeled (A, B, $\alpha$, $\beta$), rather than to the models themselves. Clearly, the models work well for defects of the spheroid type (both oblate and prolate). However, the more complex shapes require a more germane set of parameters to be modeled. A more appropriate set of defect descriptors might be the first several coefficients on a spherical harmonic expansion. Solutions of this type should be considered for future work.

## 6. ALN NETWORK MODELS

The more significant ALN models developed within the last two years for inverting crack and void defects are covered in this section and are illustrated in Figures 6.2 - 6.12. Each figure shows the element connectivity, the mathematical form of the element, a description of the input features, and the network weighting coefficients. The ALN model is the equation which relates the input feature to the modeled output parameter. In all cases shown below, the output parameter has been chosen to be a specific characteristic of the crack or void defect. One important product of the ALN synthesis procedure is that all insignificant features are eliminated from the final model. The models shown below, therefore, identify which features are significant in performing the inversion.

The network configuration of the ALN model has been adopted since very complicated nonlinear multivariant relationships can be represented in a compact form. For instance, consider the simple hypothetical network shown in Figure 6.1 and assume that each of the elements (boxes) represents the following four-term algebraic relationship of the two input variables:

$$y_1 = a_0 + a_1x_1 + a_2x_2 + a_3x_1x_2 \qquad (6.1)$$

$$y_2 = b_0 + b_1x_3 + b_2x_4 + b_3x_3x_4 \qquad (6.2)$$

$$y_3 = c_0 + c_1y_1 + c_2y_2 + c_3y_1y_2 \qquad (6.3)$$

Substituting Equation (6.1) and (6.2) into (6.3) yields:

$$\begin{aligned} y_3 = {} & c_0 + c_1(a_0 + a_1x_1 + a_2x_2 + a_3x_1x_2) \\ & + c_2(b_0 + b_1x_3 + b_2x_4 + b_2x_3x_4) \\ & + c_3(a_0 + a_1x_1 + a_2x_2 + a_3x_1x_2) \\ & \quad (b_0 + b_1x_3 + b_2x_4 + b_3x_3x_4) \end{aligned} \qquad (6.4)$$

Expansion of Equation (6.4) would yield $y_3$ as a nonlinear function of $x_1$, $x_2$, $x_3$, and $x_4$ with greater than 60 terms. Therefore, the networks

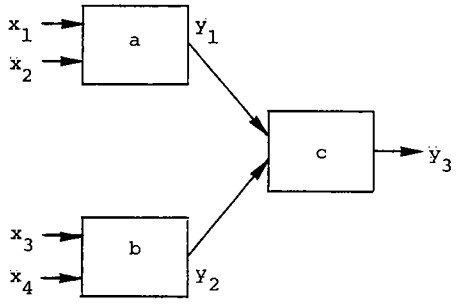


FIGURE 6.1: HYPOTHETICAL NETWORK

ALN STRUCTURE

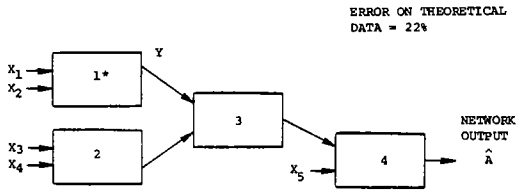


*ELEMENTAL FORM: $Y = w_0 + w_1x_1 + w_2x_2 + w_3x_1x_2 + w_4x_1^2 + w_5x_2^2 + w_6x_1^3 + w_7x_2^3$

FEATURE DESCRIPTION

| | | Mean ($\bar{X}_i$) | Sigma ($\sigma_i$) |
|---|---|---|---|
| X1: | Z-Component of the Moment Vector (Z) of the total power | .699 | .130 |
| X2: | $w_3$-Surface Coefficient of the Ripple Frequency | -.228 | .302 |
| X3: | $w_2$-Surface Coefficient of the Ripple Frequency | .755 | .714 |
| X4: | Z-Component of the Moment Vector (Z) of the Ripple Frequency | 2.61 | 1.27 |
| X5: | ATAN2 of the Ripple Frequency | 9.43 | 5.44 |

NETWORK WEIGHTING COEFFICIENTS

| ELEMENT | $w_0$ | $w_1$ | $w_2$ | $w_3$ | $w_4$ | $w_5$ | $w_6$ | $w_7$ |
|---|---|---|---|---|---|---|---|---|
| 1 | .544 | 1.240 | 1.60 | .862 | 0 | .150 | 0 | 0 |
| 2 | -.063 | .806 | .691 | .454 | .546 | 0 | .282 | .040 |
| 3 | -.172 | .878 | .704 | .454 | .168 | 0 | 0 | 0 |
| 4 | .001 | 1.012 | .034 | 0 | 0 | 0 | 0 | .091 |

FIGURE 6.2: ADAPTIVE LEARNING NETWORK TO ESTIMATE THE SEMI-MINOR AXIS "$\hat{A}$" FOR ELLIPTICAL CRACK DEFECTS

ALN STRUCTURE

ERROR ON THEORETICAL DATA = 13%

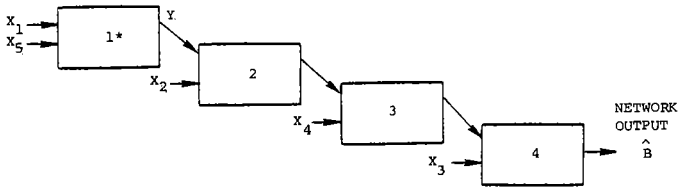


*ELEMENTAL FORM: $Y = w_0 + w_1x_1 + w_2x_2 + w_3x_1x_2 + w_4x_1^2 + w_5x_2^2 + w_6x_1^3 + w_7x_2^3$

FEATURE DESCRIPTION

| | | Mean ($\bar{X}_i$) | Sigma ($\sigma_i$) |
|---|---|---|---|
| X1: | Z-Component of the Moment Vector ($\bar{Z}$) of the Total Power | .699 | .130 |
| X2: | $w_4$-Surface Coefficient of the Ripple Frequency | .027 | .070 |
| X3: | X-Component of the Moment Vector ($\bar{X}$) of the Ripple Frequency | -.017 | .347 |
| X4: | Y-Component of the Moment Vector ($\bar{Y}$) of the Ripple Frequency | .036 | .364 |
| X5: | Z-Component of the Moment Vector ($\bar{Z}$) of the Ripple Frequency | 2.61 | 1.27 |

NETWORK WEIGHTING COEFFICIENTS

| ELEMENT | $w_0$ | $w_1$ | $w_2$ | $w_3$ | $w_4$ | $w_5$ | $w_6$ | $w_7$ |
|---|---|---|---|---|---|---|---|---|
| 1 | .245 | 1.045 | .962 | .102 | .485 | -.457 | -.315 | -.117 |
| 2 | -.015 | .943 | -.272 | 0 | 0 | 0 | 0 | .008 |
| 3 | -.107 | .956 | .052 | 0 | 0 | .107 | 0 | 0 |
| 4 | -.120 | .963 | .002 | 0 | 0 | .120 | 0 | 0 |

FIGURE 6.3: ADAPTIVE LEARNING NETWORK TO ESTIMATE THE SEMI-MAJOR AXIS "$\hat{B}$" FOR ELLIPTICAL CRACK DEFECTS

ALN STRUCTURE

ERROR ON THEORETICAL DATA = 5%

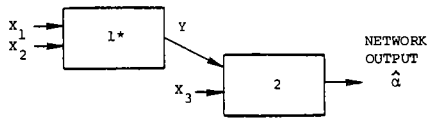


*ELEMENTAL FORM: $Y = w_0 + w_1x_1 + w_2x_2 + w_3x_1x_2 + w_4x_1^2 + w_5x_2^2 + w_6x_1^3 + w_7x_2^3$

FEATURE DESCRIPTION

| | | Mean ($\bar{X}_i$) | Sigma ($\sigma_i$) |
|---|---|---|---|
| X1: | Z-Component of the Moment Vector ($\bar{Z}$) of the Total Power | .710 | .131 |
| X2: | ATAN2 of the Total Power | 34.1 | 15.7 |
| X3: | ATAN4 of the Total Power | 90.0 | 35.5 |

NETWORK WEIGHTING COEFFICIENTS

| ELEMENT | $w_0$ | $w_1$ | $w_2$ | $w_3$ | $w_4$ | $w_5$ | $w_6$ | $w_7$ |
|---|---|---|---|---|---|---|---|---|
| 1 | .154 | -2.580 | -1.752 | 1.407 | 1.016 | 0 | .222 | 0 |
| 2 | 0 | 1.010 | .096 | 0 | 0 | 0 | 0 | 0 |

FIGURE 6.4: ADAPTIVE LEARNING NETWORK TO ESTIMATE THE POLAR ANGLE "$\hat{\alpha}$" FOR ELLIPTICAL CRACK DEFECTS

ALN STRUCTURE

ERROR ON THEORETICAL DATA = 10%

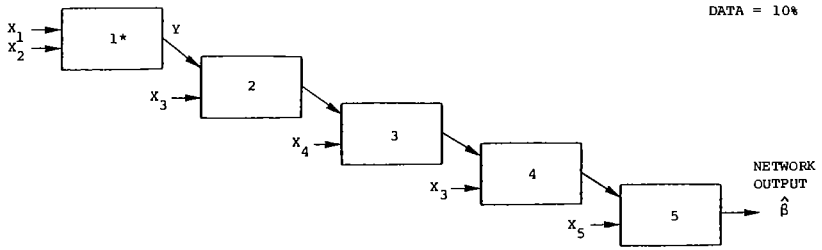


*ELEMENTAL FORM: $Y = w_0 + w_1x_1 + w_2x_2 + w_3x_1x_2 + w_4x_1^2 + w_5x_2^2 + w_6x_1^3 + w_7x_2^3$

FEATURE DESCRIPTION

| | | Mean ($\bar{x}_i$) | Sigma ($\sigma_i$) |
|---|---|---|---|
| X1: | Z-Component of the Moment Vector ($\bar{z}$) of the Total Power | .695 | .118 |
| X2: | ATAN1 of the Total Power | -9.13 | 103. |
| X3: | Y-Component of the Moment Vector ($\bar{y}$) of the Total Power | -.028 | .373 |
| X4: | $w_6$-Surface Coefficient of the Total Power | -108. | 1934. |
| X5: | X-Component of the Moment Vector ($\bar{x}$) of the Ripple Frequency | -.006 | .337 |

NETWORK WEIGHTING COEFFICIENTS

| ELEMENT | $w_0$ | $w_1$ | $w_2$ | $w_3$ | $w_4$ | $w_5$ | $w_6$ | $w_7$ |
|---|---|---|---|---|---|---|---|---|
| 1 | -.875 | - .114 | .182 | 0 | -.086 | .808 | 0 | -.204 |
| 2 | .279 | 1.207 | -.079 | -.466 | -.509 | 0 | 0 | 0 |
| 3 | .031 | 1.345 | -.404 | 0 | -.026 | 0 | -.276 | 0 |
| 4 | .032 | 1.287 | -.053 | -.357 | 0 | -.407 | 0 | 0 |
| 5 | 0 | 1.102 | -.228 | 0 | 0 | 0 | 0 | .033 |

FIGURE 6.5: ADAPTIVE LEARNING NETWORK TO ESTIMATE THE AZIMUTHAL ANGLE "$\hat{\beta}$" FOR ELLIPTICAL CRACK DEFECTS

ALN STRUCTURE

ERROR ON THEORETICAL DATA = 21%

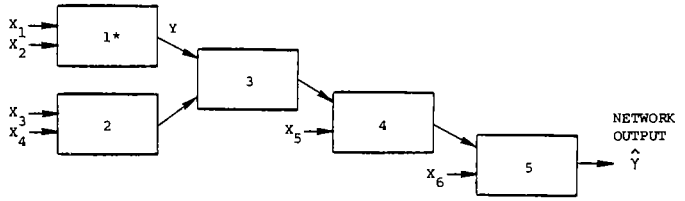


*ELEMENTAL FORM: $Y = w_0 + w_1x_1 + w_2x_2 + w_3x_1^2 + w_4x_1^2 + w_5x_2^2 + w_6x_1^3 + w_7x_2^3$

FEATURE DESCRIPTION

| | | Mean ($\bar{x}_i$) | Sigma ($\sigma_i$) |
|---|---|---|---|
| X1: | ATAN2 of the Total Power | 39.5 | 9.69 |
| X2: | ATAN2 of the Ripple Frequency | 10.6 | 4.83 |
| X3: | ATAN1 of the Total Power | -7.70 | 102. |
| X4: | X-Component of the Moment Vector ($\bar{x}$) of the Ripple Frequency | -.017 | .374 |
| X5: | ATAN4 of the Total Power | 93.2 | 38.0 |
| X6: | ATAN1 of the Ripple Frequency | 5.60 | 103. |

NETWORK WEIGHTING COEFFICIENTS

| ELEMENT | $w_0$ | $w_1$ | $w_2$ | $w_3$ | $w_4$ | $w_5$ | $w_6$ | $w_7$ |
|---|---|---|---|---|---|---|---|---|
| 1 | .128 | - .160 | 0 | 0 | -.050 | .099 | .024 | .056 |
| 2 | -.267 | .170 | - .135 | .561 | .300 | 0 | 0 | -.300 |
| 3 | -.001 | 1.162 | 1.045 | 2.945 | 0 | 0 | 0 | 0 |
| 4 | -.117 | 1.451 | .191 | 0 | 0 | .170 | -.520 | -.081 |
| 5 | .071 | .939 | - .028 | .409 | 0 | -.115 | 0 | 0 |

FIGURE 6.6: ADAPTIVE LEARNING NETWORK TO ESTIMATE THE ROTATION ANGLE "$\hat{\gamma}$" FOR ELLIPTICAL CRACK DEFECTS

ALN STRUCTURE

ERROR ON THEORETICAL
DATA = 6%

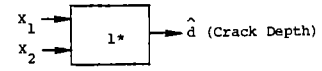


*$\hat{d} = .702X_1 - 1.588X_2$

FEATURE DESCRIPTION

| | | Mean ($\bar{X}_i$) | Sigma ($\alpha_i$) |
|---|---|---|---|
| X1: | Slope of Power Decay Across Array in Band from 0.5 to.1.5 MHz | -.155 | .015 |
| X2: | Ripple Frequency | .580 | .237 |

FIGURE 6.7: ADAPTIVE LEARNING NETWORK TO ESTIMATE THE DEPTH ($\hat{d}$) OF FREE-SURFACE CRACKS

ALN STRUCTURE

ERROR ON THEORETICAL
DATA = 9%

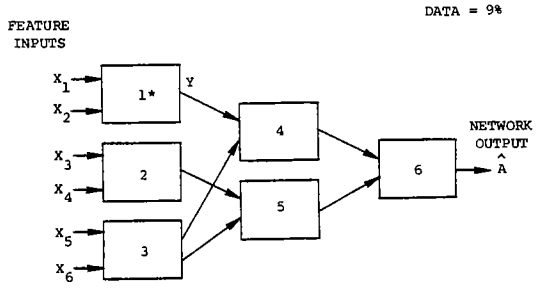


*ELEMENTAL FORM: $Y = w_0 + w_1x_1 + w_2x_2 + w_3x_1x_2 + w_4x_1^2 + w_5x_2^2$

FEATURE DESCRIPTION

$X_1$: Z-Component of the Moment Vector ($\bar{Z}$) of the First Moment of Power Spectrum

$X_2$: Z-Component of the Moment Vector ($\bar{Z}$) of Band 1 of Power Spectrum

$X_3$: X-Component of the Moment Vector ($\bar{X}$) of the First Moment of Characteristic Function

$X_4$: Z-Component of the Moment Vector ($\bar{Z}$) of the Second Moment of Characteristic Function

$X_5$: Z-Component of the Moment Vector ($\bar{Z}$) of the Total Power

$X_6$: ATAN3 of the Total Power

NETWORK WEIGHTING COEFFICIENTS

| ELEMENT | $w_0$ | $w_1$ | $w_2$ | $w_3$ | $w_4$ | $w_5$ |
|---|---|---|---|---|---|---|
| 1 | .233E+05 | -.104E+05 | -.978E+05 | .226E+05 | .116E+04 | .803E+05 |
| 2 | .973E+02 | -.388E+02 | -.701E+01 | -.548E+01 | .557E+04 | .123E+02 |
| 3 | .678E+02 | .641E+02 | -.780D+00 | -.124E+01 | .122E+02 | .118E+01 |
| 4 | .213E+02 | .142E+00 | .265E+00 | -.304E-03 | .170E-02 | .904E-03 |
| 5 | -.149E+03 | .170E+01 | .596E+00 | -.550E-03 | .195E-02 | .747E-03 |
| 6 | .416E+01 | .608E+00 | .307E+00 | .291E-03 | 0 | 0 |

FIGURE 6.8: ADAPTIVE LEARNING NETWORK TO ESTIMATE SIZE PARAMETER "$\hat{A}$" FOR SPHEROIDAL DEFECTS

ALN STRUCTURE

ERROR ON THEORETICAL DATA = 8%

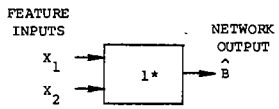


*ELEMENTAL FORM: $\hat{B} = w_0 + w_1x_1 + w_2x_2 + w_3x_1x_2 + w_4x_1^2 + w_5x_2^2$

FEATURE DESCRIPTION

$X_1$: Z-Component of the Moment Vector ($\bar{Z}$) of the First Moment of Power Spectrum

$X_2$: Z-Component of the Moment Vector ($\bar{Z}$) of Band 1 of Power Spectrum

NETWORK WEIGHTING COEFFICIENTS

| ELEMENT | $w_0$ | $w_1$ | $w_2$ | $w_3$ | $w_4$ | $w_5$ |
|---|---|---|---|---|---|---|
| 1 | -.162E+04 | .793E+03 | .400E+04 | -.367E+03 | -.804E+02 | -.346E+04 |

FIGURE 6.9: ADAPTIVE LEARNING NETWORK TO ESTIMATE SIZE PARAMETER "$\hat{B}$" FOR SPHEROIDAL DEFECTS

ALN STRUCTURE

ERROR ON THEORETICAL DATA = 5%

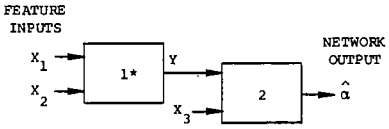


*ELEMENTAL FORM: $Y = w_0 + w_1x_1 + w_2x_2 + w_3x_1x_2 + w_4x_1^2 + w_5x_2^2$

FEATURE DESCRIPTION

$X_1$: ATAN3 of the Total Power

$X_2$: ATAN4 of the Total Power

$X_3$: ATAN2 of the Total Power

NETWORK WEIGHTING COEFFICIENTS

| ELEMENT | $w_1$ | $w_2$ | $w_3$ | $w_4$ | $w_5$ | $w_6$ |
|---|---|---|---|---|---|---|
| 1 | .137E+03 | -.151E+01 | -.910E+00 | .224E-01 | -.169E-03 | -.507E-02 |
| 2 | .609E+01 | .115E+01 | -.445E+00 | -.264E-02 | -.174E-02 | .680E-02 |

FIGURE 6.10: ADAPTIVE LEARNING NETWORK TO ESTIMATE ORIENTATION PARAMETER "$\hat{\alpha}$" FOR SPHEROIDAL DEFECTS

ALN STRUCTURE

ERROR ON THEORETICAL DATA = 1%

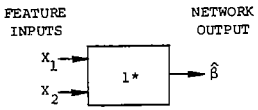


*ELEMENTAL FORM: $\hat{\beta} = w_0 + w_1x_1 + w_2x_2 + w_3x_1x_2 + w_4x_1^2 + w_5x_2^2$

FEATURE DESCRIPTION

$X_1$: ATAN4 of the First Moment of Characteristic Function

$X_2$: ATAN1 of the Total Power

NETWORK WEIGHTING COEFFICIENTS

| ELEMENT | $w_0$ | $w_1$ | $w_2$ | $w_3$ | $w_4$ | $w_5$ |
|---|---|---|---|---|---|---|
| 1 | -.576E+00 | .402E+00 | .101E+01 | -.124E-03 | -.821E-01 | -.291E-04 |

FIGURE 6.11: ADAPTIVE LEARNING NETWORK TO ESTIMATE ORIENTATION PARAMETER "$\hat{\beta}$" FOR SPHEROIDAL DEFECTS

ALN STRUCTURE

ERROR ON THEORETICAL DATA = 0%

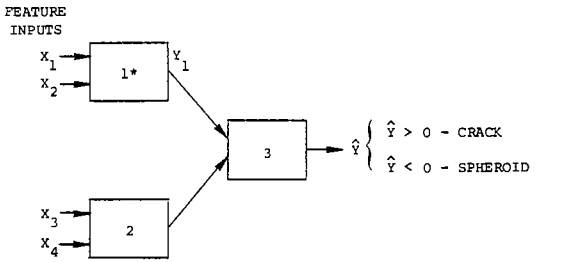


*ELEMENTAL FORM: $Y_1 = w_0 = w_1x_1 + w_2x_2 + w_3x_1x_2 + w_4x_1^2 + w_5x_2^2$

FEATURE DESCRIPTION

$X_1$: Z-Component of the Moment Vector ($\bar{Z}$) of the Power Spectral First Moment

$X_2$: Z-Component of the Moment Vector ($\bar{Z}$) of the Low to High Power Ratio

$X_3$: Y-Component of the Moment Vector ($\bar{Y}$) of the Power Spectral Standard Deviation

$X_4$: Z-Component of the Moment Vector ($\bar{Z}$) of the Power Spectral Standard Deviation

NETWORK WEIGHTING COEFFICIENTS

| ELEMENT | $w_0$ | $w_1$ | $w_2$ | $w_3$ | $w_4$ | $w_5$ |
|---|---|---|---|---|---|---|
| 1 | -.592E+02 | .305E+02 | .112E+03 | -.309E+02 | -.372E+01 | -.431E+02 |
| 2 | .353E+01 | .322E+02 | -.324E+03 | -.238E+05 | .238E+05 | .513E+04 |
| 3 | -.303E+00 | .613E+00 | .463E+00 | -.890E-01 | .216E+00 | .173E+00 |

FIGURE 6.12: ADAPTIVE LEARNING NETWORK TO DISCRIMINATE TWO-DIMENSIONAL (CRACK-LIKE) DEFECTS FROM THREE-DIMENSIONAL (VOID-LIKE) DEFECTS

shown below can, in some cases, represent many thousands of terms with only a small number of coefficients.

The networks shown in Figures 6.2 - 6.7 are the elliptical and free-surface crack models and have normalized coefficients. All of the input and output variables were scaled by removing the mean ($\bar{x}_i$) and dividing by the standard deviation ($\sigma_i$). These scaling values are shown next to each input variable. In order to implement the networks on new data observations, the computed feature values must be scaled by $x_i$ and $\sigma_i$ in the following manner:

$$x_i' = \frac{x_i - \bar{x}_i}{\sigma_i}$$

where

$x_i$ = the $i^{th}$ spectral feature

$\bar{x}_i$ = mean feature value

$\sigma_i$ = standard deviation of feature

$x_i'$ = input to network

Figures 6.2 and 6.3 show the ALN models which estimate the semiminor (A) and semimajor (B) axis of the elliptical crack defect. Note that, in each case, four of the five features selected were "ripple frequency" features. The ripple frequency is the single most important feature for determining the defect size. It was, therefore, quite natural for these features to be selected.

Figures 6.4 - 6.6 show the ALN models for estimating the three elliptical crack orientation angles $\alpha$, $\beta$, and $\gamma$, respectively. Most of the features selected for these models were total power features. It has been observed that the defect orientation is highly related to the total power spatial distribution. The flat surface of an elliptical crack acts similar to a mirror, reflecting energy in the direction opposite to that of the direction of incidence. The position of this highly directed "specular" reflection yields much information about the angles $\alpha$ and $\beta$. The moment vector ($\bar{x}$, $\bar{y}$, $\bar{z}$) attempts to locate the position of maximum energy, hence, locates the specular reflection.

Figure 6.7 illustrates the ALN model to determine the depth of free-surface cracks. The equation is a linear combination of only two features. The ripple frequency feature measures the time delay between the tip diffracted wave and the corner reflection.

Figures 6.8 - 6.11 illustrate the four oblate spheroid models to estimate the defect's size (A and B) and orientation ($\alpha$ and $\beta$). The void models were trained on theoretical data of the low ka regime. This means that the defect is small compared to the wavelength of the incident beam. When ka is small (<5), information pertaining to the size of the defect can be found in the low frequency portion of the spectrum. The networks shown in Figures 6.8 and 6.9 support this fact. Most of the features selected measure shifts in the spectral energy, or percent of low frequency energy. The void models to estimate $\alpha$ and $\beta$ (Figures 6.10 and 6.11) indicate, as for elliptical cracks, that spatial total power distribution is key in estimating the defect's orientation.

Figure 6.12 shows the Adaptive Learning Network to discriminate crack defects from voids. Four spectral features selected as shown. If the network output is positive, the indicated class is of the crack type. A negative model output is indicative of a void.

REFERENCES


1. Mucciardi, A.N., R. Shankar, M.F. Whalen, "Application of Adaptive Learning Networks to NDE Methods", Interdisciplinary Program for Quantitative Flaw Definition, Special Report, Third Year Effort, June 1977, p. 176.

2. Whalen, M.F., A.N. Mucciardi, "Inversion of Physically Recorded Ultrasonic Waveforms Using Adaptive Learning Network Trained On Theoretical Data", Interdisciplinary Program for Quantitative Flaw Definition, Special Report, Fourth Year Effort, June 30, 1978, pp. 55-80.

3. Whalen, M.F., L.J. O'Brien, A.N. Mucciardi, "Application of Adaptive Learning Networks for the Characterization of Two-Dimensional and Three-Dimensional Defects in Solids", Interdisciplinary Program for Quantitative Flaw Definition, Special Report, Fifth Year Effort, submitted Oct. 1979.

4. Adler, L., "Measurement of Scattering from Interior and Surface Cracks", Interdisciplinary Program for Quantitative Flaw Definition, Interim Report, Mar. 31, 1980, pp. 123-137.

5. Adler L., J.D. Achenbach, "Elastic Wave Diffraction by Elliptical Cracks", submitted for publication in Journal of Nondestructive Evaluation.

6. Achenbach, J.D., A.K. Gautesen, D.A. Mendelsohn, "Ray Analysis of Surface-Wave Interaction with an Edge Crack", IEEE Transactions Sonics and Ultrasonics, Vol. SU-27, No. 3.

7. Mendelsohn, D.A., A.D. Achenbach, L.M. Keer, "Scattering of Elastic Waves by a Surface-Breaking Crack", WAVE MOTION, 2, in press.

8. Achenbach, J.D., "Direct and Inverse Methods for Scattering by Cracks at High Frequencies", Interdisciplinary Program for Quantitative Flaw Definition, Interim Report, 1980.

9. Personal communication between J. Martin and M. F. Whalen.

Paul Gammel (J.P.L.): I would like to know if your system depends on deconvolution to move the transducer signature.

Tony Mucciardi (Adaptronics): No. You can either convolve the theoretical resonse with the transducer response, or deconvolve the experimental response from the transducer response to make the experiment resemble the theory. It's more general in the latter case.

Paul Gammell: What was done in your case?

Tony Muccardi: All the results have been presented with the transducer response deconvolved from the experimental data. This approach is quite pleasing because of independence from the transducer. Of course, it's quite possible to go the other way, too.

James Krumhansl, Chairman (NSF): Thank you, we will now proceed to the final paper.